Energy & Environmental Science

ROYAL SOCIETY OF CHEMISTRY

PAPER

View Article Online
View Journal | View Issue



Cite this: *Energy Environ. Sci.*, 2024, **17**, 6844

# C-shaped *ortho*-benzodipyrrole-based acceptors with different electronic effects of top substituents for as-cast green-solvent processed high-performance organic solar cells†

Yufei Gong, ‡[ab] Tianwei Zou,‡[ab] Xiaojun Li,*[ab] Shucheng Qin,[ab] Guangpei Sun,[ab] TongLing Liang,[bc] Ruimin Zhou,[d] Jianqi Zhang,[be] Jinyuan Zhang,[ab] Lei Meng,[ab] Zhixiang Wei[be] and Yongfang Li*[abf]

The milestone achievement of organic solar cells (OSCs) in recent years relies on the rapid development of A–DA′D–A type small molecule acceptors (SMAs) with C-shaped molecular geometry. Recently, C-shaped *ortho*-benzodipyrrole (*o*-BDP)-based SMAs without fused electron-withdrawing triazole or thiadiazole units exhibit strong near-infrared absorption. However, the effects of the top substituents on the photovoltaic performance of this type of SMA is still unclear. In this work, three SMAs, namely, FF24-Cl, FM24-Cl and MM24-Cl, with the top substituents of difluorine, fluorine and methyl, and dimethyl, respectively, were synthesized based on C-shaped *o*-BDP. From FF24-Cl to FM24-Cl and then to MM24-Cl, the gradually decreased electron-withdrawing ability of the top substituents leads to an orderly enhanced intramolecular charge transfer (ICT) effect, resulting in red-shifted absorption and a reduced bandgap ($E_g$). In addition, the nature of the top substituents has a significant effect on the homo-molecular interaction between the SMAs and the hetero-molecular interaction of the SMAs with polymer donors. Finally, due to the suitable molecular packing and appropriate phase separation modulated by the top substituents, an FM24-Cl-based OSC processed by non-halogenated solvent without any extra treatment exhibits elevated exciton dissociation, enhanced charge transport and suppressed carrier recombination, achieving a higher power conversion efficiency (PCE) of 18.30%. As far as we know, this efficiency is the highest value for the OSCs fabricated by applying the simplest processing method, which is important for the future application of OSCs. In particular, the energy loss ($E_{loss}$) of SMA-based OSCs gradually decreases with the increased electron-donating ability of the top substituents, and an MM24-Cl-based OSC exhibits the lowest $E_{loss}$ of 0.47 eV among the OSCs with PCE exceeding 17%. This work indicates that the top substituents play an important role in regulating the physicochemical and photovoltaic properties of the C-shaped *o*-BDP-based SMAs and may provide new opportunities for obtaining OSCs with lower $E_{loss}$ and higher PCE.

Received 6th June 2024,
Accepted 1st August 2024

DOI: 10.1039/d4ee02467b

rsc.li/ees

## Broader context

Organic solar cells (OSCs) have attracted great attention owing to their advantages of lightweightness and flexibility. The power conversion efficiency (PCE) of OSCs has rapidly increased to approximately 20% recently, benefitting from the development of the A–DA′D–A type small molecule acceptor (SMA) Y6 and its derivatives based on a C-shaped *ortho*-benzodipyrrole (*o*-BDP) with fused electron-withdrawing (A′) unit. However, the effects of the top substituents on the

[a] *Beijing National Laboratory for Molecular Sciences, CAS Key Laboratory of Organic Solids, Institute of Chemistry, Chinese Academy of Sciences, Beijing 100190, China. E-mail: lixiaojun@iccas.ac.cn, liyf@iccas.ac.cn*
[b] *School of Chemical Science, University of Chinese Academy of Sciences, Beijing 100049, China*
[c] *Center for Physicochemical Analysis and Measurement, Institute of Chemistry, Chinese Academy of Sciences, Beijing 100190, China*
[d] *College of Chemistry and Green Catalysis Center, Zhengzhou University, Zhengzhou 450001, China*
[e] *CAS Key Laboratory of Nanosystem and Hierarchical Fabrication, National Center for Nanoscience and Technology, Beijing 100190, China*
[f] *Laboratory of Advanced Optoelectronic Materials, College of Chemistry, Chemical Engineering and Materials Science, Soochow University, Suzhou 215123, China*

† Electronic supplementary information (ESI) available. CCDC 2333674–2333676 (**FF24-Cl, FM24-Cl** and **MM24-Cl**). For ESI and crystallographic data in CIF or other electronic format see DOI: **https://doi.org/10.1039/d4ee02467b**

‡ These authors contributed equally to this work.

photovoltaic performance of C-shaped *o*-BDP-based SMAs is still unclear. In addition, these OSCs typically require rigorous fabrication conditions and tedious optimization processes, with halogenated solvents, additives, and thermal annealing appearing to be necessary options, which undoubtedly pose serious challenges to the future commercialization. Therefore, we designed and synthesized three C-shaped *o*-BDP-based SMAs, namely, FF24-Cl, FM24-Cl and MM24-Cl to systematically investigate the effects of the top substituents on the physicochemical properties of SMAs and demonstrated that the C-shaped *o*-BDP-based SMA with moderate electron-withdrawing top substituents can achieve a higher PCE of 18.30% for the OSCs processed by non-halogenated solvent without any extra treatment. This inspires us to develop as-cast green-solvent processed high-performance OSCs *via* molecular modification in the future.

## 1. Introduction

In recent years, significant breakthroughs have been made in the power conversion efficiency (PCE) of organic solar cells (OSCs)[1–6] mainly due to the rapid development of C-shaped A–DA′D–A type small molecule acceptors (SMAs).[7–11] Thus far, the PCE of OSCs based on A–DA′D–A type SMA Y6[12] and its derivatives has exceeded 19%.[13–15] Inspired by the outstanding photovoltaic performance of A–DA′D–A type SMAs, great efforts are underway to modify the structure and explain the mechanism behind the superiority of this type of SMA.[16–18] However, the effects of the A′ unit on the photovoltaic performance of A–DA′D–A type SMAs is still not clear, and only few reports are available. Some C-shaped *ortho*-benzodipyrrole (*o*-BDP)-based SMAs with weaker electron-withdrawing A′ units exhibit lower energy loss ($E_{loss}$) were reported.[19–21] The stronger electron-withdrawing A′ unit may increase the reorganization energy from the singlet ground state ($S_0$) to the first singlet excited state ($S_1$), which is not conducive to exciton diffusion and leads to enhanced non-radiative decay.[22,23] Moreover, it was observed that some C-shaped SMAs without a fused electron-withdrawing unit on the *o*-BDP unit possess strong near-infrared absorption and narrow optical bandgap ($E_g^{opt}$) comparable to Y6.[24,25] Recently, Cheng *et al.* found that this type of SMA can also achieve high photovoltaic performance under certain processing conditions.[26] It is obvious that the electronic effect of top substituents on C-shaped *o*-BDP-based SMAs has a significant effect on photovoltaic performance, but further studies are still lacking; especially, research on converting top substituents from electron-withdrawing groups to electron-donating groups has not been reported. Hence, it is necessary to systematically investigate the effects of the top substituents

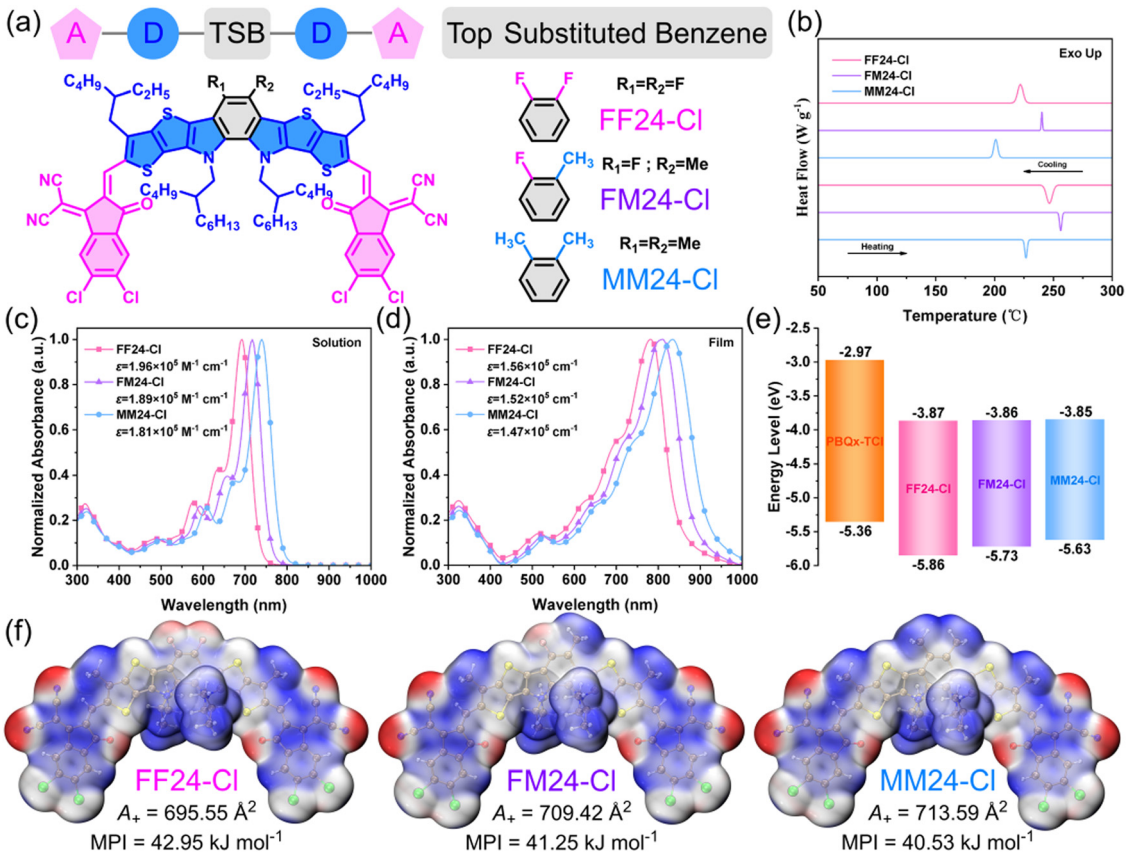


Fig. 1 (a) Chemical structures of FF24-Cl, FM24-Cl and MM24-Cl (TSB represents "top substituted benzene"). (b) DSC curves of FF24-Cl, FM24-Cl and MM24-Cl under nitrogen atmosphere at a heating rate of 10 °C min$^{-1}$ from 50 °C to 300 °C. Normalized absorption spectra of FF24-Cl, FM24-Cl and MM24-Cl (c) in *o*-xylene solution and (d) in thin film. (e) Energy level diagram of polymer donor and SMAs in OSCs. (f) ESP diagrams of FF24-Cl, FM24-Cl and MM24-Cl.

on the physicochemical properties of SMAs to further improve the photovoltaic performance of SMAs.

It is interesting that for the C-shaped SMAs without a fused electron-withdrawing unit, the benzene core unit (referring to the benzene ring in the *o*-BDP unit) provides two additional top substitution sites to further modify the structure and improve the photovoltaic performance of the *o*-BDP-based SMAs. Based on this strategy, we can investigate the effects of the top substituents on the physicochemical and photovoltaic properties of the C-shaped *o*-BDP-based SMAs. Therefore, we designed and synthesized three SMAs FF24-Cl, FM24-Cl and MM24-Cl (Fig. 1a) with the top substituents of difluorine, fluorine and methyl, dimethyl, respectively. The electron density of the difluoro-benzene core in FF24-Cl severely decreases due to the disubstitution of fluorine with strong electron-withdrawing ability, while the electron density of the dimethyl-benzene core in MM24-Cl slightly increases due to the disubstitution of methyl with weak electron-donating ability. Due to the partial cancellation of the electronic effects of fluorine and methyl, the electron density of FM24-Cl moderately decreases. Therefore, through the systematic studies of the SMAs, we can gain knowledge about the effects of the top substituents on the benzene core unit on the photovoltaic performance of the C-shaped *o*-BDP-based SMAs.

We found that from FF24-Cl to FM24-Cl and then to MM24-Cl, the decreased electron-withdrawing ability of the benzene core unit led to an enhanced intramolecular charge transfer (ICT) effect, resulting in a red-shifted absorption and a reduced bandgap ($E_g$). Moreover, the asymmetric substitution in FM24-Cl with a moderate electron-withdrawing ability endows the SMA showing unique crystallization behavior and additional charge transfer, which is beneficial for its electrical performance. The top substituents on the benzene core unit also have a profound effect on the interaction and miscibility of the SMAs with the polymer donor, which can be effectively improved by decreasing the electron-withdrawing ability of the benzene core unit. Due to the suitable molecular packing and appropriate phase separation, the FM24-Cl-based OSC with PBQx-TCl as donor exhibits elevated exciton dissociation, enhanced charge transport and suppressed carrier recombination, achieving a higher PCE of 18.30%, which is the highest value for the OSCs processed by non-halogenated solvent without any extra treatment. We found that as the electron-withdrawing ability of the top substituents on the benzene core unit is weakened or its electron-donating ability is strengthened, the $E_{loss}$ of the corresponding OSCs gradually decreases. Among them, the MM24-Cl-based OSC exhibits a significantly reduced $E_{loss}$ of 0.47 eV, which is the smallest value among OSCs with PCE exceeding 17%. These results indicate that the moderate electron-withdrawing top substituents (or fused ring) could be beneficial to the higher photovoltaic performance of the SMAs, and the electron-donating top substituents could reduce $E_{loss}$ of the SMA-based OSCs, inspiring us to achieve high comprehensive performance OSCs *via* molecular modification in the future.

## 2. Results and discussion

The chemical structures of three SMAs FF24-Cl, FM24-Cl and MM24-Cl are shown in Fig. 1a, and the detailed synthesis processes are described in Scheme S1 in ESI.† All the compounds were fully characterized (Fig. S1–S6 in ESI†) by nuclear magnetic resonance (NMR) spectroscopy and matrix-assisted laser desorption/ionization Fourier-transform ion cyclotron resonance mass spectrometry (MALDI-FTICR-MS). The SMAs exhibit good solubility in non-halogenated solvents, such as toluene and *o*-xylene, ensuring their processability as photovoltaic materials in OSCs. The thermal stability of the SMAs was characterized by thermogravimetric analysis (TGA) under a nitrogen atmosphere, and the results are shown in Fig. S7 and Table S1 in ESI.† The thermal decomposition temperature ($T_d$, the temperature corresponding to 5% weight loss) of FF24-Cl, FM24-Cl and MM24-Cl are 376 °C, 373 °C and 370 °C, respectively, which are higher than that of Y6 and its derivatives (*ca.* 320 °C),[27] ensuring sufficient thermal stability as photovoltaic materials in OSCs. Meanwhile, the crystallization behavior of the SMAs was investigated by differential scanning calorimetry (DSC) under a nitrogen atmosphere, and the results are shown in Fig. 1b and Table S1 in ESI.† All of them exhibit obvious first-order phase change peaks, revealing the existence of crystal structures. The melting/crystallizing point ($T_m/T_c$) of FF24-Cl, FM24-Cl and MM24-Cl are 247/222 °C, 256/240 °C and 227/201 °C, respectively. Generally, the asymmetric substitution may disrupt the molecular orientation and stacking due to symmetry destruction. However, surprisingly, FM24-Cl has the highest $T_m$ and $T_c$, showing unique crystallization behavior.

The ultraviolet-visible (UV-Vis) absorption spectra of the SMAs in the *o*-xylene solution and thin film are shown in Fig. 1c and d. The detailed parameters of the optical properties are summarized in Table 1. The maximum absorption peak wavelengths ($\lambda_{max}^{sol.}$) of FF24-Cl, FM24-Cl and MM24-Cl in solution are 693 nm, 717 nm and 740 nm, respectively, indicating that the electronic effect of the top substituents can significantly influence the absorption, and the absorption gradually red-shifts with the decreased electron-withdrawing ability (or increased electron-donating ability) of the top substituents. Meanwhile, to further reveal the role of the top substituents of the SMAs in absorption, BT24-Cl (a derivative of Y6) was synthesized (Fig. S8 in ESI†). It is worth noting that FM24-Cl without a typical fused electron-withdrawing triazole or thiadiazole unit possesses absorption comparable to BT24-Cl (Fig. S9 in ESI,† $\lambda_{max}^{sol.}$ is 725 nm), and MM24-Cl exhibits further red-shifted absorption and enhanced absorbance in the long-wavelength region, which once again proves that the electron-withdrawing top substituents (or fused ring) may be unnecessary for the SMAs to obtain more red-shifted absorption. From solution to film, the $\lambda_{max}^{film}$ of FF24-Cl, FM24-Cl and MM24-Cl red-shifts to 782 nm, 811 nm and 835 nm, with the corresponding $\Delta\lambda_{max}^{s\rightarrow f}$ of 89 nm, 94 nm and 95 nm, respectively. According to the $\lambda_{onset}^{film}$, $E_g^{opt}$ can be obtained as 1.46 eV, 1.39 eV and 1.34 eV for FF24-Cl, FM24-Cl and MM24-Cl, respectively ($E_g^{opt}$ of BT24-Cl is 1.39 eV), indicating that the

 

Table 1 Optical properties and electronic energy levels of FF24-Cl, FM24-Cl and MM24-Cl

| Acceptor | $\lambda_{max}^{sol.}$ [nm] | $\lambda_{max}^{film}$ [nm] | $\Delta\lambda_{max}^{s\rightarrow f}$ [nm] | $\lambda_{onset}^{film}$ [nm] | RAI [a.u.] | $\Delta\lambda_{Stokes}$ [nm] | $E_g^{opt}$ [eV] | $E_{HOMO}$ [eV] | $E_{LUMO}$ [eV] | $E_g^{ec}$ [eV] |
|---|---|---|---|---|---|---|---|---|---|---|
| FF24-Cl | 693 | 782 | 89 | 851 | 1.119 | 48 | 1.46 | −5.86 | −3.87 | 1.99 |
| FM24-Cl | 717 | 811 | 94 | 889 | 1.129 | 43 | 1.39 | −5.73 | −3.86 | 1.87 |
| MM24-Cl | 740 | 835 | 95 | 927 | 1.131 | 39 | 1.34 | −5.63 | −3.85 | 1.78 |

decreased electron-withdrawing ability of the top substituents can attain a reduced $E_g^{opt}$. To better understand the effect of the top substituents on the aggregation behavior of the SMAs, the temperature-dependent UV-Vis absorption spectra of the SMAs in the *o*-xylene solution were measured (Fig. S10 in ESI†). The ratio of the $I(\lambda_{max}^{sol.})$ at a specific temperature to that at 100 °C is defined as the relative aggregation intensity (RAI),[28] and the slope of the curve can reflect the aggregation rate (Fig. S11 in ESI†). When the temperature gradually decreases from 100 °C to 40 °C, MM24-Cl has the highest RAI and faster aggregation rate, while FF24-Cl has the lowest RAI and the slowest aggregation rate, which indicates that molecular pre-aggregation in solution is enhanced with the decreased electron-withdrawing ability of the top substituents. Moreover, the ratio of the $I(\lambda_{0\rightarrow1}^{sol.})$ to the $I(\lambda_{0\rightarrow1}^{sol.})$ is regarded as an important parameter for evaluating the intensity of J aggregation, and a smaller value indicates stronger J aggregation.[29] Regardless of whether at high or low temperatures, this value decreases in the order of FF24-Cl, FM24-Cl and MM24-Cl, proving that the molecular J aggregation in solution enhances with the decreased electron-withdrawing ability of the top substituents (Fig. S11 in ESI†). In addition, the degree of exciton delocalization (DED) can be judged by the ratio of the exciton bandwidth ($E_w$) to the nuclear relaxation energy ($SE_v$).[30] The former is related to the intermolecular excitonic coupling and is considered a measure of exciton delocalization, which is equal to twice the energy difference between $E(\lambda_{0\rightarrow0}^{sol.})$ and $E(\lambda_{0\rightarrow0}^{film})$. The latter represents the energy released when the molecule relaxes to the minimum of the excited state potential surface and is considered a measure of exciton localization. The Huang–Rhys factor ($S$) describes the strength of electron–phonon coupling, which can be calculated by the ratio of the $I(\lambda_{0\rightarrow1}^{sol.})$ to the $I(\lambda_{0\rightarrow0}^{sol.})$. The vibrational energy ($E_v$) is the energy separation between $E(\lambda_{0\rightarrow1}^{sol.})$ and $E(\lambda_{0\rightarrow0}^{sol.})$. The DED values of FF24-Cl, FM24-Cl and MM24-Cl were calculated to be 5.95, 6.43 and 6.45, respectively, indicating that exciton delocalization is more significant in FM24-Cl and MM24-Cl (Table S2, ESI†). Turning attention to the photoluminescence (PL) spectra (Fig. S12 in ESI†), FF24-Cl, FM24-Cl and MM24-Cl films show PL peaks at 830 nm, 854 nm and 874 nm, respectively; thus, the Stokes shifts ($\Delta\lambda_{Stokes}$) of the SMAs gradually decrease with the decreased electron-withdrawing ability of the top substituents (Table 1). The $\Delta\lambda_{Stokes}$ is caused by the elimination of excess energy by vibrational relaxation and internal conversion and is closely related to the Förster energy transfer rate in OSCs.[31] Therefore, the smaller $\Delta\lambda_{Stokes}$ of FM24-Cl and MM24-Cl may indicate that they possess an increased exciton diffusion rate and reduced non-radiative recombination, which is beneficial for suppressing $E_{loss}$ in OSCs.

The highest occupied molecular orbital energy level ($E_{HOMO}$) and the lowest unoccupied molecular orbital energy level ($E_{LUMO}$) of the SMAs were measured by cyclic voltammetry (CV),[32] and the corresponding electrochemical cyclic voltammograms are shown in Fig. S13 in ESI.† The $E_{HOMO}/E_{LUMO}$ values of FF24-Cl, FM24-Cl and MM24-Cl calculated from the onset oxidation/reduction potentials ($\varphi_{ox}/\varphi_{red}$) in the cyclic voltammograms are −5.86/−3.87 eV, −5.73/−3.86 eV, and −5.63/−3.85 eV, and the corresponding electrochemical bandgap ($E_g^{ec}$) are 1.99 eV, 1.87 eV, and 1.78 eV, respectively, as shown in Fig. 1e and Table 1. These results indicate that with the increased electron-donating ability of the top substituents, the $E_{HOMO}$ up-shifts significantly whereas the $E_{LUMO}$ remains almost unchanged, which agrees with the reduced $E_g$.

To understand the effect of the top substituents on the physicochemical properties of FF24-Cl, FM24-Cl and MM24-Cl, density functional theory (DFT) calculation was carried out for the SMAs (Table S3 in ESI†). To simplify the calculation, the outer and inner side-chains of the SMAs were replaced with methyl and isobutyl, respectively. The simulated UV-Vis absorption spectra of the SMAs are shown in Fig. S14 in ESI.† All of them exhibit strong absorption in the range of 400–550 nm and 600–850 nm, which can be attributed to the π–π* transition and ICT transition, respectively. In addition, the $\lambda_{max}^{cal}$ gradually red-shifts from FF24-Cl to FM24-Cl and then to MM24-Cl (Table S3 in ESI†), which is consistent with the experimental results. The calculated bandgap ($E_g^{cal}$) of FF24-Cl, FM24-Cl and MM24-Cl are 2.17 eV, 2.12 eV and 2.08 eV, respectively (Fig. S15 and Table S3 in ESI†), and this trend is consistent with $E_g^{opt}$ and $E_g^{ec}$. Referring to the electrostatic surface potential (ESP) diagrams (Fig. 1f and Table S3 in ESI†), the blue area with a positive ESP value ($A_+$) gradually expands from 695.55 Å$^2$ for FF24-Cl to 709.42 Å$^2$ for FM24-Cl and then to 713.59 Å$^2$ for MM24-Cl, with the decreased molecular polarity index (MPI) of 42.95 kJ mol$^{-1}$, 41.25 kJ mol$^{-1}$ and 40.53 kJ mol$^{-1}$, which helps to improve the interaction and miscibility of the SMAs with polymer donor (Fig. S16 in ESI†), thereby decreasing phase separation of the SMAs with polymer donor in the active layer.[33]

In addition, the excited state properties of the SMAs were investigated through time-dependent DFT (TD-DFT) calculation.[34] Fig. 2a shows the hole–electron distribution (green represents the hole and blue represents the electron) of the SMAs from $S_0$ to $S_1$. The hole is mainly distributed on the core unit, and the electron is mainly distributed on the conjugate extensions. The hole–electron overlap index $S_r$ is used to evaluate the hole–electron overlap. The larger the value, the higher the degree of overlap. The results show that the $S_r$ index gradually decreases from FF24-Cl to FM24-Cl and then to MM24-Cl (Table S3 in ESI†), indicating that the decreased

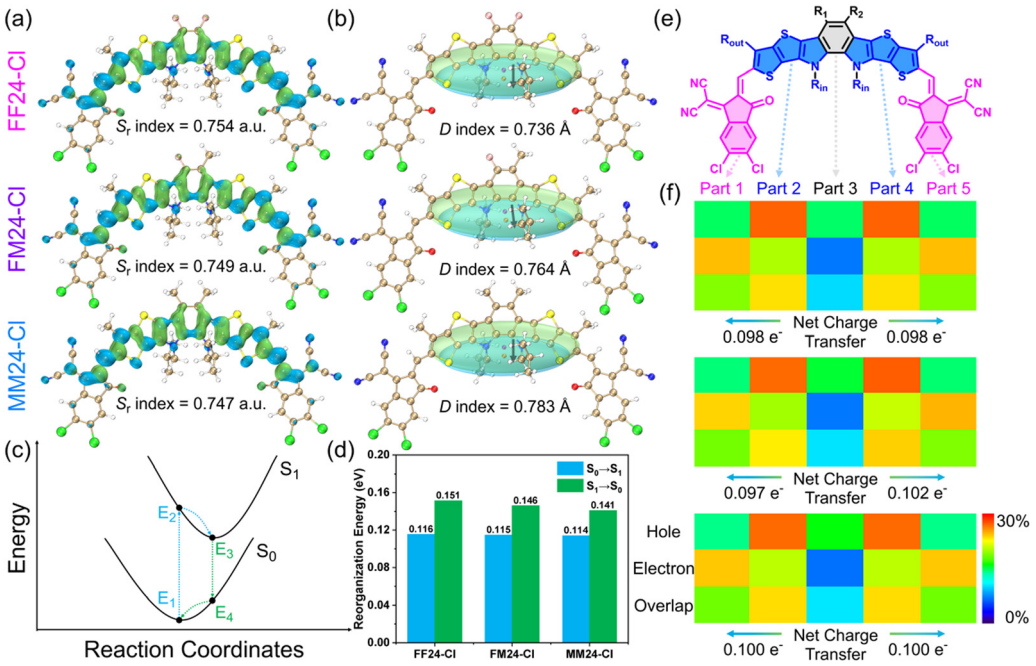


Fig. 2 (a) Hole–electron distribution (green represents the hole and blue represents the electron) of FF24-Cl, FM24-Cl and MM24-Cl from $S_0$ to $S_1$. (b) Equivalent description of hole–electron distribution. (c) Illustration of the related transitions between $S_0$ and $S_1$ during the photoelectric conversion processes. (d) Reorganization energies for $S_0 \rightarrow S_1$ and $S_1 \rightarrow S_0$ in FF24-Cl, FM24-Cl and MM24-Cl. (e) Schematic of the SMA divided into five segments. (f) Contribution of each part of the molecule to hole, electron and hole–electron overlap.

electron-withdrawing ability of the top substituents can mitigate the degree of hole–electron overlap, which plays a positive role in reducing the $E_{loss}$ of OSCs.[35]

To intuitively display the hole–electron distribution in various directions, Gaussian functions were used to equivalently describe the spatial distribution ($C_{hole}$, $C_{ele}$), and the hole–electron centroid spacing index $D$ was calculated (Fig. 2b). The results show that the $D$ index gradually increases from FF24-Cl to FM24-Cl and then to MM24-Cl (Table S3 in ESI†), indicating that the decreased electron-withdrawing ability of the top substituents can lead to more significant hole–electron separation, which contributes to the red-shifted absorption and reduced $E_g$.[36] Because holes and electrons often exist in the form of exciton pairs in organic semiconductors, the hole–electron Coulomb attractive energy ($E_{coul}$) is an important parameter for measuring the difficulty of hole–electron separation. Surprisingly, FM24-Cl with asymmetric top substituents has the smallest $E_{coul}$ of 2.664 eV (Table S3 in ESI†), even smaller than many high photovoltaic performance SMAs (*ca.* 2.706 eV), which may be attributed to the promotion of hole–electron separation by symmetry destruction.[37] As shown in Fig. 2c and d, the reorganization energy for $S_0 \rightarrow S_1$ transition ($\lambda_{S_0 \rightarrow S_1}$) is related to the geometry relaxation in $S_1$ after light absorption, and the reorganization energy for the $S_1 \rightarrow S_0$ transition ($\lambda_{S_1 \rightarrow S_0}$) is associated with non-radiative decay from $S_1$ to $S_0$. Their sum corresponds to the reorganization energy for exciton diffusion. From FF24-Cl to FM24-Cl and then to MM24-Cl, the reorganization energy gradually decreases (especially $\lambda_{S_1 \rightarrow S_0}$), which indicates that the decreased electron-withdrawing ability of the top substituents is conducive to exciton diffusion, leading to suppressed non-radiative decay (Table S3 in ESI†).

The SMAs were divided into five segments, with the terminal groups as parts 1 and 5, the conjugate extensions as parts 2 and 4, and the core unit as part 3 (Fig. 2e). To further quantitatively illustrate the hole–electron distribution, the contribution of each part to hole, electron, hole–electron overlap and hole–electron difference ($\Delta C$) were calculated, and the corresponding heat maps were drawn for data visualization.[38] As shown in Fig. 2f and Tables S4–S6 in ESI,† the contribution of conjugate extensions to the hole is the most significant, accounting for over 53%, and the corresponding matrix elements are red. While the contribution of terminal groups to electrons is the most significant, accounting for nearly 49%, and the corresponding matrix elements are orange. The $\Delta C$ of the core unit and conjugate extensions are negative, while the $\Delta C$ of the terminal groups is positive, indicating that electrons flow from the core unit and conjugate extensions to the terminal groups. From FF24-Cl to FM24-Cl and then to MM24-Cl, the contribution of part 3 (core unit) to the hole increases, while the contribution to the electron decreases, which is closely related to the electronic effect of the top substituents. It is worth noting that the asymmetric top substituents have a comprehensive impact on the hole–electron distribution of the entire molecule,[39] that is the hole contribution rate of the conjugate extension and the electron contribution rate of the terminal group near the methyl side are higher than the corresponding values near the fluorine side, and the corresponding matrix

 

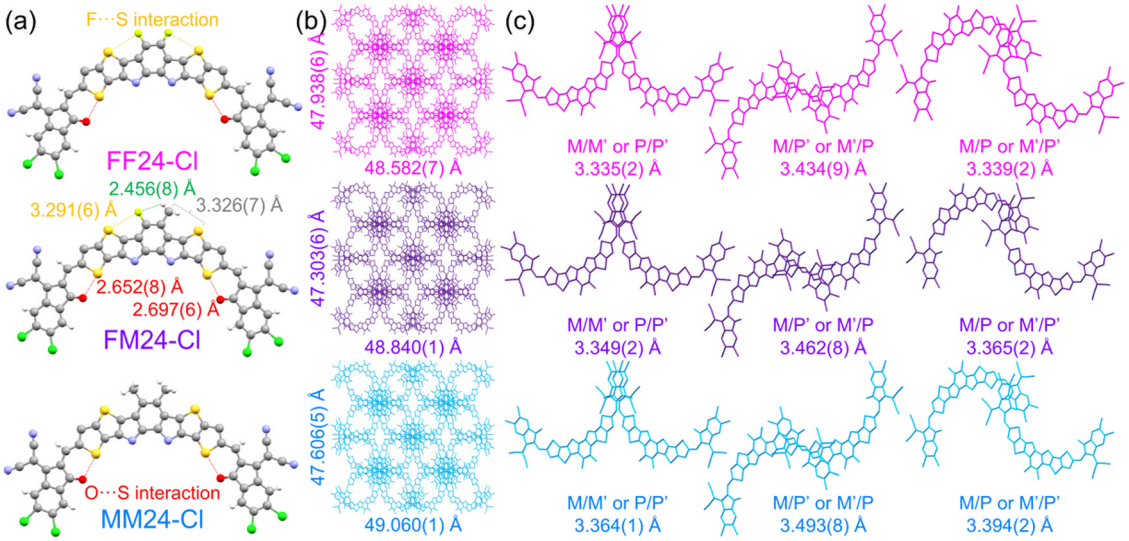


Fig. 3 (a) Monomolecular geometry from the top view of FF24-Cl, FM24-Cl and MM24-Cl. (b) Single crystal packing diagrams from the top view of FF24-Cl, FM24-Cl and MM24-Cl (the hydrogen atoms and alkyl chains are omitted for clarity). (c) Three stacking modes of FF24-Cl, FM24-Cl and MM24-Cl (the π–π space for each mode is given).

elements are significantly red-shifted. Through further quantitative calculation, it can be concluded that the net charge transfer amounts on the fluorine side and methyl side of FM24-Cl are 0.097 $e^-$ and 0.102 $e^-$, respectively. This difference may have a positive impact on the intermolecular interaction. Overall, the top substituents on the benzene core unit affect the charge transfer process of the entire molecule by regulating the distribution of holes and electrons on the conjugate extensions and terminal groups.

To acquire more structural information on molecular packing variations of FF24-Cl, FM24-Cl and MM24-Cl, an X-ray single-crystallographic analysis was presented (Fig. S17 in ESI†). Single crystals of the SMAs were cultivated using a solvent diffusion method with methanol as a poor solvent and chloroform as a good solvent. The detailed parameters of the crystallographic properties are summarized in Table S7 in ESI† and deposited at the Cambridge Crystallographic Data Center (CCDC). As shown in Fig. 3a, the monomolecular geometry of FF24-Cl, FM24-Cl and MM24-Cl are C-shaped, consistent with Y6 and its derivatives. Considering the van der Waals radii of hydrogen, fluorine and sulfur atoms are 1.20 Å, 1.47 Å and 1.80 Å, respectively, it can be found that multiple non-covalent interactions exist between the fluorine atoms at the core unit and the sulfur atoms at the conjugate extensions (orange dotted lines) as well as the oxygen atoms at the terminal groups and the sulfur atoms at the conjugate extensions (red dotted lines). For FM24-Cl, there is an additional non-covalent interaction between the fluorine atom and hydrogen atom of the methyl group on the core unit (green dotted line). As shown in Fig. 3b, unlike Y6 and its derivatives displaying three-dimensional grid-like patterns with a single type of elliptical void, the SMAs of FF24-Cl, FM24-Cl and MM24-Cl exhibit more intricate patterns formed by four layers of repeating molecules and possess three stacking modes in adjacent P (P′) and M (M′) enantiomers, including terminal group to terminal group in a near mirror symmetric dimer (A/A, Mode 1), between two conjugate extensions with a terminal group in the near central symmetric dimer (D–A/A–D, Mode 2) and terminal group to terminal group in the near central symmetric dimer (A/A, Mode 3), which can provide multiple charge transport channels (Fig. 3c and Fig. S18, ESI†). Furthermore, distinct differences in the details of the stacking modes of the SMAs can be observed. The FF24-Cl, FM24-Cl and MM24-Cl single crystals contain the π–π stacking between the terminal group and terminal group with the π–π space of 3.335/3.349/3.364 Å (Mode 1, M/M′ or P/P′) and 3.339/3.365/3.394 Å (Mode 3, M/P or M′/P′), as well as the π–π stacking between terminal group and conjugate extension with the π–π space of 3.434/3.462/3.493 Å (Mode 2, M/P′ or M′/P), respectively. Overall, the π–π space gradually increases in the order of FF24-Cl, FM24-Cl and MM24-Cl.

To evaluate the photovoltaic performance of the SMAs, the wide-bandgap polymer PBQx-TCl[40] (Fig. S19 in ESI†) with complementary absorption (Fig. S20 in ESI†) and suitable energy level (Fig. 1e) was selected as the donor to fabricate the OSCs with the conventional device architecture of ITO/PEDOT:PSS/active layer/PDINN/Ag, and the detailed fabrication methods are described in ESI.† It is worth noting that all the OSCs in this work are fabricated using non-halogenated *o*-xylene as the solvent without the treatment of additive and thermal annealing. This not only avoids the environmental pollution caused by halogenated solvents and additives but also enhances morphology stability and reduces optimization complexity.[41–43] The photovoltaic performance parameters of these OSCs were measured under the standard test conditions of a solar energy conversion system (AM 1.5G, 100 mW $cm^{-2}$). The current density–voltage (*J*–*V*) curves of the optimized OSCs are shown in Fig. 4a, and the corresponding photovoltaic

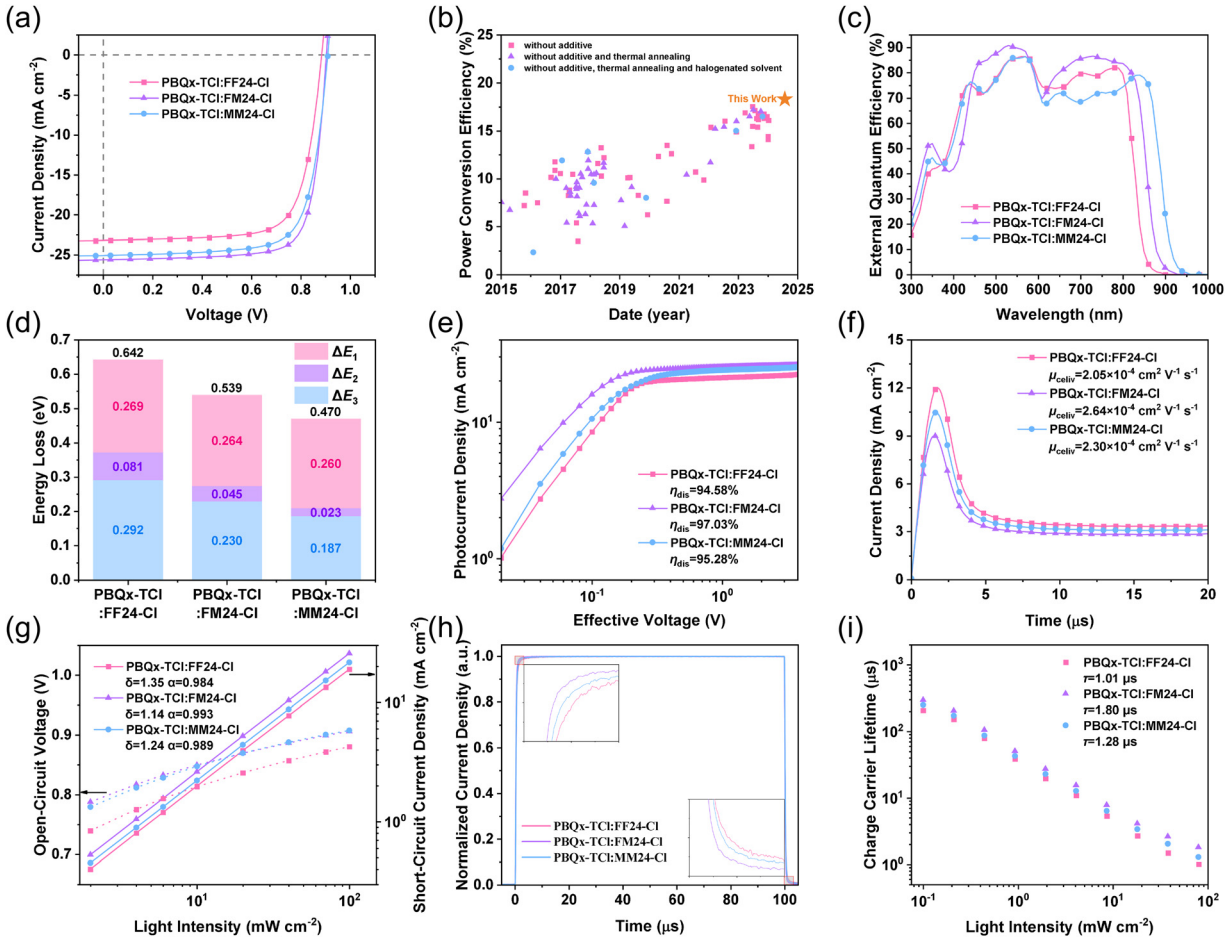


Fig. 4 (a) $J$–$V$ curves of the optimized OSCs with PBQx-TCl as the donor and FF24-Cl/FM24-Cl/MM24-Cl as the acceptor under the irradiation of AM 1.5G, 100 mW cm$^{-2}$. (b) Statistical diagram of the PCE of the OSCs processed by a non-halogenated solvent without any extra treatment reported in the literature. (c) EQE curve, (d) statistical diagram of $E_{loss}$, (e) $J_{ph}$–$V_{eff}$ curve, (f) photo-CELIV curve, (g) $J_{sc}$/$V_{oc}$–$P_{light}$ curve, (h) normalized TPC curve in response to a 100 μs white light pulse and (i) charge carrier lifetime curve under different $P_{light}$ values obtained from TPV experiment of the OSC based on PBQx-TCl:FF24-Cl/FM24-Cl/MM24-Cl.

Table 2 Photovoltaic performance parameters of the optimized OSCs with PBQx-TCl as the donor and FF24-Cl/FM24-Cl/MM24-Cl as the acceptor fabricated using non-halogenated *o*-xylene as the solvent without the treatment of additive and thermal annealing under an irradiation of AM 1.5G, 100 mW cm$^{-2}$

| Device | $V_{oc}$ [V] | $J_{sc}$ [mA cm$^{-2}$] | $J_{cal}$[a] [mA cm$^{-2}$] | FF [%] | PCE[b] [%] |
|---|---|---|---|---|---|
| PBQx-TCl:FF24-Cl | 0.886 (0.884 ± 0.001) | 23.24 (22.93 ± 0.18) | 22.56 | 74.82 (74.62 ± 0.14) | 15.40 (15.12 ± 0.14) |
| PBQx-TCl:FM24-Cl | 0.905 (0.904 ± 0.001) | 25.66 (25.36 ± 0.18) | 24.91 | 78.85 (78.61 ± 0.16) | 18.30 (18.02 ± 0.14) |
| PBQx-TCl:MM24-Cl | 0.911 (0.910 ± 0.001) | 25.13 (24.78 ± 0.23) | 24.40 | 75.84 (75.60 ± 0.15) | 17.35 (17.05 ± 0.18) |

[a] The values were determined *via* integration of the EQE curves. [b] The average was calculated based on 20 individual devices.

performance parameters are listed in Table 2 for a clear comparison. The open-circuit voltage ($V_{oc}$) of the FF24-Cl-, FM24-Cl- and MM24-Cl-based OSCs increases from 0.886 V to 0.905 V and then to 0.911 V with the decreased electron-withdrawing ability of the top substituents. This is attributed to the decreased $E_{loss}$, which is discussed in detail later. Among them, the FM24-Cl-based OSC has the highest short-circuit current density ($J_{sc}$) and fill factor (FF), achieving a higher PCE of 18.30%, which is the highest value for the OSCs processed by non-halogenated solvent without any extra treatment, as far as we know (Fig. 4b and Table S8 in ESI†). Based on the same fabrication methods, the MM24-Cl-based OSC demonstrates a medium PCE of 17.35% (Table 2), while the FF24-Cl- and BT24-Cl-based OSCs show lower PCE of 15.40% (Tables 2) and 15.39% (Table S9 in ESI†), respectively.

For the OSCs based on Y6 and its derivatives, the processing by halogenated solvent and the treatment of additive and thermal annealing is the key to optimizing active layer

 

morphology for improving photovoltaic performance. A non-halogenated solvent typically has lower solubility for the active layer materials and higher boiling points that prolong the evaporation time, exacerbating the aggregation of the donor and acceptor during the film-forming process,[44] which generally requires an additive to regulate and obtain a bicontinuous interpenetrating network with an appropriate domain size, unless there is strong interaction and good miscibility between the donor and acceptor. If an additive is used, thermal annealing must be carried out to avoid residue accelerating degradation and deteriorating morphology, which has a negative impact on the durability of OSCs.[45] In other words, if there is strong interaction and good miscibility between donor and acceptor, the active layer processed by the non-halogenated solvent does not undergo excessive phase separation, and there is no need for further adjustment through additive and thermal annealing. This may explain why the halogenated solvent, additive and thermal annealing can be abandoned in the corresponding OSCs fabrication while showcasing higher performance compared to other devices. Meanwhile, the photovoltaic performance parameters of these OSCs with the treatment of thermal annealing are listed in Table S10 (ESI†). Compared with those in Table 2, the almost unchanged device performances confirm that the active layers of these OSCs achieve relatively balanced and thermally stable phase separation without any extra treatment. Moreover, the durabilities of these OSCs under light irradiation and heat treatment are shown in Fig. S21 and S22 (ESI†). After being continuously irradiated (100 mW $cm^{-2}$) for 400 hours or being continuously heated (65 °C) for 200 hours, these OSCs still maintain nearly 95% of their initial PCE. These results indicate that as-cast green-solvent-processed OSCs possess good stability. Furthermore, to explore the universality of this type of SMA, two common polymers, PM6 and D18, were selected as donors to match FM24-Cl, and the corresponding photovoltaic performance parameters of the OSCs are fabricated using non-halogenated *o*-xylene as the solvent without the treatment of additive and thermal annealing, as listed in Table S11 (ESI†). It can be observed that these OSCs also show good photovoltaic performance with a PCE of 16–17%.

Fig. 4c shows the external quantum efficiency (EQE) curves of these OSCs, with a gradually red-shifted photo-response range. The integrated current density ($J_{cal}$) from the EQE curves of the FF24-Cl-, FM24-Cl- and MM24-Cl-based OSCs are 22.56 mA $cm^{-2}$, 24.91 mA $cm^{-2}$ and 24.40 mA $cm^{-2}$, respectively. Compared with FM24-Cl, MM24-Cl has a more red-shifted absorption, but the MM24-Cl-based OSC exhibits slightly lower $J_{cal}$, which can be attributed to the lower absorbance in the range of 600–800 nm (Fig. 1d) and weaker photo-response caused by inappropriate donor–acceptor phase separation. The $J_{cal}$ values of the corresponding OSCs are well matched with the $J_{sc}$ obtained from *J–V* curves, indicating the reliability of the photovoltaic performance measurements.

Because FF24-Cl, FM24-Cl and MM24-Cl have very similar $E_{LUMO}$, the different $V_{oc}$ values of the corresponding OSCs may originate from the different $E_{loss}$, which can be divided into three parts: $E_{loss} = \Delta E_1 + \Delta E_2 + \Delta E_3$,[46,47] and the corresponding results are shown in Fig. 4d and Table 3. $\Delta E_1$ is inevitable in all solar cells and depends on the $E_g$ of the material at a specific spectrum and temperature ($\Delta E_1 = E_g - qV_{oc}^{SQ}$, where $V_{oc}^{SQ}$ is the output voltage in the Shockley–Queisser limit model). Here, $\Delta E_1$ of the FF24-Cl/FM24-Cl/MM24-Cl-based OSC is 0.269/0.264/0.260 eV. $\Delta E_2$ refers to the radiative recombination loss below the $E_g$ and is mainly contributed by the lower-lying CT state ($\Delta E_2 = qV_{oc}^{SQ} - qV_{oc}^{Rad}$), which corresponds to the driving force required for exciton dissociation. From the FF24-Cl- to FM24-Cl- and then to MM24-Cl-based OSC, $\Delta E_2$ decreases sharply from 0.081 eV to 0.045 eV and 0.023 eV, respectively (Fig. S23 and S24 in ESI†). $\Delta E_3$ is the non-radiative recombination loss ($\Delta E_3 = qV_{oc}^{Rad} - qV_{oc}^{Cal} = -kT\ln EQE_{EL}$, where $EQE_{EL}$ is the radiative quantum efficiency of the OSC when the charge carrier is injected in dark conditions). This part of $E_{loss}$ is ascribed from the non-radiative decay of the CT state to the ground state and the recombination of the separated free charges. As discussed in the optical properties of the SMAs, from FF24-Cl to FM24-Cl and then to MM24-Cl, the $\Delta\lambda_{Stokes}$ gradually decreases, which indicates that the non-radiative recombination rate may decrease with the increased electron-donating ability of the top substituents. Therefore, compared to FF24-Cl, the FM24-Cl-/MM24-Cl-based OSC exhibits a higher $EQE_{EL}$ of $1.36 \times 10^{-4}$/$7.28 \times 10^{-4}$ (Fig. S25 in ESI†), resulting in a smaller $\Delta E_3$ of 0.230/0.187 eV due to the reduced non-radiative recombination. Because both the driving force required for exciton dissociation and non-radiative recombination are significantly reduced, the $E_{loss}$ in the FM24-Cl-/MM24-Cl-based OSC is dramatically decreased, as small as 0.539/0.470 eV. It is worth noting that the latter is the smallest value among the OSCs with PCE exceeding 17% (Fig. S26 and Table S12 in ESI†).

To gain insight into the reasons for the different photovoltaic performances of these OSCs, the exciton dissociation, charge transport and recombination characteristics were explored. Fig. 4e shows the curves of the photocurrent density ($J_{ph}$) *versus* the effective voltage ($V_{eff}$) of these OSCs, which are plotted to investigate the exciton dissociation ($\eta_{dis}$) behavior. The $\eta_{dis}$ of the FM24-Cl-based OSC is 97.03%, which is higher than the corresponding value of 94.58%/95.28% for the FF24-Cl-/MM24-Cl-based OSC, resulting in higher $J_{sc}$ and FF. The

Table 3 $E_{loss}$ of the OSC based on PBQx-TCl:FF24-Cl/FM24-Cl/MM24-Cl

| Device | $E_g$ [eV] | $qV_{oc}^{SQ}$ [eV] | $qV_{oc}^{Rad}$ [eV] | $qV_{oc}^{Cal}$ [eV] | $EQE_{EL}$ [a.u.] | $\Delta E_1$ [eV] | $\Delta E_2$ [eV] | $\Delta E_3$ [eV] | $E_{loss}$ [eV] |
|---|---|---|---|---|---|---|---|---|---|
| PBQx-TCl:FF24-Cl | 1.521 | 1.252 | 1.171 | 0.879 | $1.28 \times 10^{-5}$ | 0.269 | 0.081 | 0.292 | 0.642 |
| PBQx-TCl:FM24-Cl | 1.452 | 1.188 | 1.143 | 0.913 | $1.36 \times 10^{-4}$ | 0.264 | 0.045 | 0.230 | 0.539 |
| PBQx-TCl:MM24-Cl | 1.386 | 1.126 | 1.103 | 0.916 | $7.28 \times 10^{-4}$ | 0.260 | 0.023 | 0.187 | 0.470 |

elevated exciton dissociation of the FM24-Cl-based OSC may result from the synergistic effect of the larger $D$ index and smaller $E_{coul}$ of the molecule,[48] as well as the suitable phase separation of the PBQx-TCl:FM24-Cl blend film.

The charge transport properties were investigated by applying the space charge limited current (SCLC) method with the device architecture of ITO/PEDOT:PSS/Active Layer/$MoO_3$/Ag for hole mobility ($\mu_h$) and ITO/ZnO/Active Layer/PDINN/Ag for electron mobility ($\mu_e$) measurement. The corresponding curves are exhibited in Fig. S27 in ESI,† and the detailed parameters are listed in Table S13 in ESI† for a clear comparison. According to the equation $J = 9\varepsilon_0\varepsilon_r\mu V^2/8d^3$, the FM24-Cl-based OSC shows higher and more balanced $\mu_h/\mu_e$ of $4.09 \times 10^{-4}/5.07 \times 10^{-4}$ $cm^2\ V^{-1}\ s^{-1}$ than that of $2.51 \times 10^{-4}/3.64 \times 10^{-4}$ $cm^2\ V^{-1}\ s^{-1}$ for the FF24-Cl-based OSC and that of $3.30 \times 10^{-4}/4.38 \times 10^{-4}$ $cm^2\ V^{-1}\ s^{-1}$ for the MM24-Cl-based OSC. Besides, the photoinduced charge carrier extraction by linearly increasing voltage (Photo-CELIV) was measured to further explore the charge carrier generation and transport behaviors of these OSCs under work conditions. Fig. 4f illustrates the recorded Photo-CELIV curves of these OSCs with charge carrier mobility ($\mu_{celiv}$) of $2.05 \times 10^{-4}$ $cm^2\ V^{-1}\ s^{-1}$, $2.64 \times 10^{-4}$ $cm^2\ V^{-1}\ s^{-1}$ and $2.30 \times 10^{-4}$ $cm^2\ V^{-1}\ s^{-1}$. These results indicate that the FM24-Cl-based OSC has better charge transport properties than those of the FF24-Cl-/MM24-Cl-based OSC, which is an important reason for its superior photovoltaic performance.

The light intensity ($P_{light}$) dependence values of $V_{oc}$ and $J_{sc}$ were measured to evaluate the charge recombination behaviors of the corresponding OSCs (Fig. 4g). In principle, $V_{oc} \propto (\delta kT/e)\ln P_{light}$, where $k$, $T$ and $e$ are Boltzmann constant, absolute temperature and elementary charge. The $\delta$ determines whether the process is dominated by bimolecular recombination ($\delta \to 1$) or trap-assisted recombination ($\delta \to 2$). According to Fig. 4g, the $\delta$ were calculated to be 1.35 for the FF24-Cl-based OSC, 1.14 for the FM24-Cl-based OSC and 1.24 for the MM24-Cl-based OSC, indicating that there is the least trap-assisted recombination in the FM24-Cl-based OSC. In addition, according to the $J_{sc} \propto P_{light}^{\alpha}$, $\alpha$ represents the degree of bimolecular recombination, and $\alpha$ closer to 1 means less bimolecular recombination. The FM24-Cl-based OSC exhibits a higher $\alpha$ of 0.993 than that of 0.984/0.989 for the FF24-Cl-/MM24-Cl-based OSC (Fig. 4g), which indicates that bimolecular recombination is most significantly suppressed in the FM24-Cl-based OSC.

To further understand the charge transport and recombination properties in these OSCs, transient photocurrent (TPC) and transient photovoltage (TPV) experiments were performed, and the corresponding results are depicted in Fig. 4h and i. In the TPC test (Fig. 4h), the OSC generates a transient current due to an optical pulse. The faster response of the FM24-Cl-based OSC compared to that of the FF24-Cl-/MM24-Cl-based OSC reveals that the former has higher charge mobility and fewer traps. In the TPV test (Fig. 4i), the charge carrier lifetime ($\tau$) can be calculated by $V(t) = V_{oc} + \Delta V \times \exp(-t/\tau)$, where $\Delta V$ is the voltage increment caused by a small light pulse. The $\tau$ of the FM24-Cl-based OSC is 1.80 μs, which is longer than that of 1.01/1.28 μs for the FF24-Cl-/MM24-Cl-based OSC, suggesting the less charge recombination in the FM24-Cl-based OSC. These results indicate that the appropriate electron-withdrawing ability of

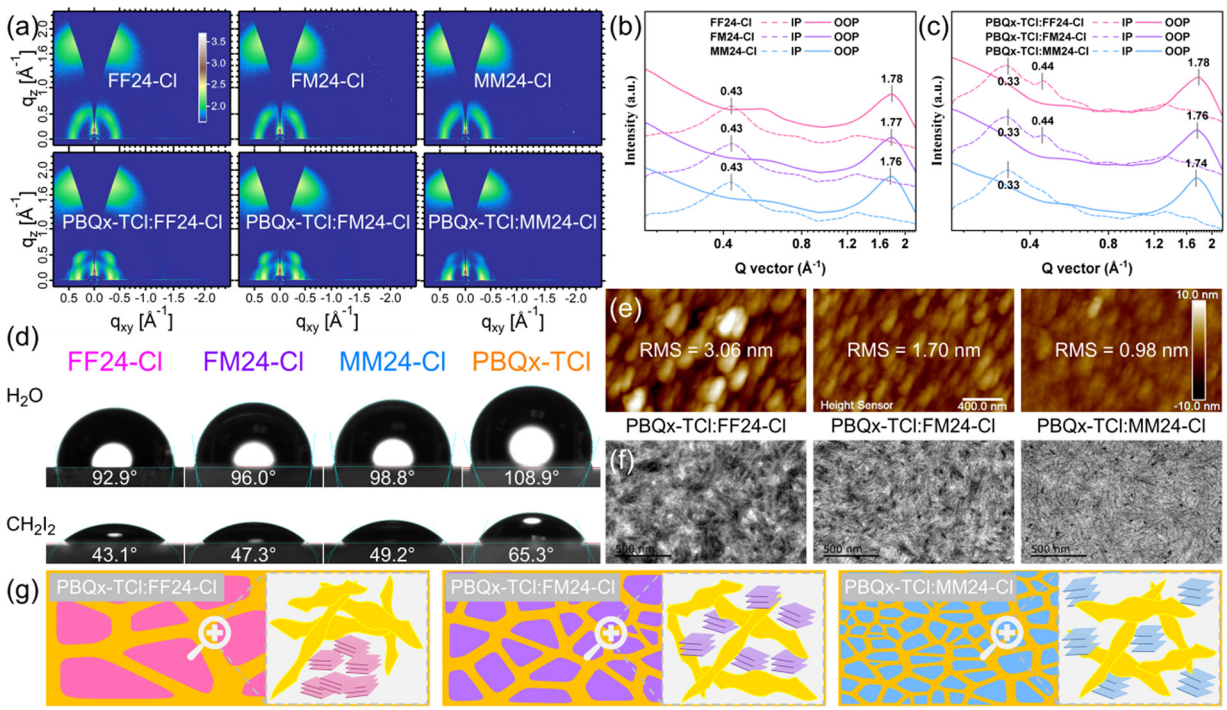


Fig. 5 (a) Two-dimensional GIWAXS patterns and the corresponding line-cuts in the IP (dashed lines) and OOP (solid lines) directions of (b) neat film based on FF24-Cl/FM24-Cl/MM24-Cl and (c) blend film based on PBQx-TCl:FF24-Cl/FM24-Cl/MM24-Cl. (d) CA test results of FF24-Cl, FM24-Cl, MM24-Cl and PBQx-TCl. (e) AFM height images, (f) TEM images and (g) schematic of the blend film based on PBQx-TCl:FF24-Cl/FM24-Cl/MM24-Cl.

 

the top substituents enables the FM24-Cl-based OSC with elevated exciton dissociation, enhanced charge transport and suppressed carrier recombination, which eventually contributes to the superior photovoltaic performances.

To elucidate the effect of the top substituents on molecular orientation and stacking, grazing-incidence wide-angle X-ray scattering (GIWAXS) experiments[49] were conducted on the neat and blend films based on these materials. The two-dimensional GIWAXS patterns and the corresponding line-cuts in the in-plane (IP) and out-of-plane (OOP) directions are shown in Fig. 5a–c. The detailed parameters are listed in Tables S14–S15 in ESI† for clear comparison. For all neat films, the diffraction peaks at 0.43 $Å^{-1}$ are indexed as (100) peaks, corresponding to the IP lamellar stacking with a lattice constant of 14.63 Å. The diffraction peaks of FF24-Cl at 1.78 $Å^{-1}$, FM24-Cl at 1.77 $Å^{-1}$ and MM24-Cl at 1.76 $Å^{-1}$ are identified as (010) peaks, associated with the π–π stacking in the OOP direction, which suggests that the SMAs are predominantly "face-on" orientated in neat films. The π–π stacking distance values of FF24-Cl, FM24-Cl and MM24-Cl are 3.53 Å, 3.55 Å and 3.58 Å, with the crystalline coherence lengths (CCL) of 14.53 Å, 15.08 Å and 15.38 Å, respectively. The increased π–π stacking distance of the SMAs can be attributed to the increased steric hindrance of the top substituents. However, the presence of a steric hindrance does not affect the order of molecular packing. The corresponding increased CCL of the SMAs indicates that the order of molecular packing in a thin film is improved with the decreased electron-withdrawing ability of the top substituents, which is consistent with the results obtained from absorption. The increased order of molecular packing of FF24-Cl, FM24-Cl and MM24-Cl may be mainly due to the enhanced molecular interaction caused by hole–electron separation. For all blend films, the diffraction peaks at 0.33 $Å^{-1}$ and 0.44 $Å^{-1}$ can be assigned to the IP lamellar stacking of the donor and acceptor, respectively (Fig. S28 in ESI†). It is worth noting that from the FF24-Cl to the FM24-Cl and then to the MM24-Cl-based blend film, the (100) peak of the SMAs at 0.44 $Å^{-1}$ gradually weakens or even disappears (Fig. 4c). This indicates that with the decreased electron-withdrawing ability of the top substituents, the influence of the polymer donor on the molecular accumulation of the SMAs gradually increases, and this change is mainly due to the enhanced interaction and miscibility between donor and acceptor,[50,51] which is discussed in detail later.

To investigate the effect of the top substituents on the morphology change in the active layer based on PBQx-TCl:FF24-Cl/FM24-Cl/MM24-Cl, the surface energy (SE) and the Flory–Huggins interaction parameter ($\chi$) of these materials were calculated from the contact angle (CA) test (Fig. 5d and Table S16 in ESI†). The SEs of FF24-Cl, FM24-Cl, MM24-Cl and PBQx-TCl are 38.14 mN $m^{-1}$, 36.00 mN $m^{-1}$, 35.19 mN $m^{-1}$ and 26.32 mN $m^{-1}$, respectively. The closer SE means the better miscibility between donor and acceptor. According to the empirical formula $\chi = K\left(\sqrt{\gamma_D} - \sqrt{\gamma_A}\right)^2$, where $K$ is a constant and $\gamma_D/\gamma_A$ denotes the SE of the donor/acceptor,[52] the $\chi$ of the blend films of PBQx-TCl:FF24-Cl, PBQx-TCl:FM24-Cl and PBQx-TCl:MM24-Cl were calculated to be 1.09 $K$, 0.76 $K$ and 0.64 $K$, respectively. The gradually decreased $\chi$ of the blend films means the enhanced miscibility between donor and acceptor with the decreased electron-withdrawing ability of the top substituents. This may be due to the expanded interaction area and the closer molecular polarity between the donor and acceptor, as confirmed by the DFT calculation. This trend is also reflected in the atomic force microscopy (AFM) and transmission electron microscopy (TEM) images (Fig. 5e and f) of the blend films based on these materials. The AFM images show that the root mean square (RMS) roughness decreases from 3.06 nm for the PBQx-TCl:FF24-Cl blend film to 1.70 nm for the PBQx-TCl:FM24-Cl blend film and then to 0.98 nm for the PBQx-TCl:MM24-Cl blend film. This can be explained by the enhanced miscibility between the donor and acceptor, resulting in decreased phase separation and a smoother surface of the blend film. In the TEM images, from the FF24-Cl to the FM24-Cl and then to the MM24-Cl-based film, the messy cluster disappears with the appearance of uniform dispersion, and a clear nanoscale fiber structure can be observed. Combined with the results of CA, AFM and TEM, the miscibility between donor and acceptor in the blend film can be effectively improved by decreasing the electron-withdrawing ability of the top substituents (Fig. 5g). As is well known, excessive phase separation can suppress exciton dissociation, while inadequate phase separation increases exciton recombination and restricts charge transfer.[53] Therefore, benefiting from the most suitable phase separation of PBQx-TCl:FM24-Cl blend film, higher $J_{sc}$ and FF of the OSC were obtained compared to those of the OSCs based on PBQx-TCl:FF24-Cl and PBQx-TCl:MM24-Cl.

However, the MM24-Cl-based OSC does not achieve the highest efficiency due to the inappropriate morphology caused by the over-miscibility between the donor and acceptor. It is worth noting that the MM24-Cl-based OSC exhibits a significantly higher $V_{oc}$ with a similar $\lambda_{onset}^{film}$ to Y6 due to very low $E_{loss}$. Minimizing $E_{loss}$ is crucial in the pursuit of high photovoltaic performance OSCs, which is also a significant challenge in SMAs design. Therefore, in pace with the increased electron-donating ability of the top substituents, the $E_{loss}$ of the corresponding OSCs gradually decreases, which becomes a very interesting design direction for the SMAs. We will strive to suppress the over-miscibility of MM24-Cl with suitable polymer donors through molecular modification, and design more SMAs by regulating the electronic effect of the top substituents in the C-shaped SMAs.

## 3. Conclusions

In this work, we designed and synthesized three C-shaped *o*-BDP-based SMAs FF24-Cl, FM24-Cl and MM24-Cl with the decreased electron-withdrawing ability of the top substituents on the benzene core unit. We demonstrated that the decreased electron-withdrawing ability (or increased electron-donating ability) of the top substituents is beneficial for the red-shifted

absorption and reduced $E_g$ of the SMAs and that the nature of the top substituents in the C-shaped SMAs has a significant effect on the homo-molecular interaction between the SMAs and the hetero-molecular interaction of the SMAs with the polymer donor. Benefiting from suitable molecular packing and appropriate phase separation regulated by the top substituents, the FM24-Cl-based OSC with PBQx-TCl as the donor exhibits elevated exciton dissociation, enhanced charge transport and suppressed carrier recombination, achieving a higher PCE of 18.30%, which is the highest value for the OSCs processed by non-halogenated solvent without any extra treatment. Specifically, with the increased electron-donating ability of the top substituents, the $E_{loss}$ of the corresponding OSCs gradually decreases. The MM24-Cl-based OSC exhibits a significantly reduced $E_{loss}$ of 0.47 eV, which is the smallest value among the OSCs with PCE exceeding 17%. Therefore, adjusting the electron-withdrawing ability of the top substituents in the C-shaped *o*-BDP-based SMAs is an effective strategy for achieving low $E_{loss}$, providing new opportunities for obtaining OSCs with lower $E_{loss}$ and higher PCE through further molecular modification in the future.

## Author contributions

Y. G. synthesized and characterized the SMAs FF24-Cl, FM24-Cl and MM24-Cl, and T. Z. optimized the OSCs based on the SMAs. X. L. designed and guided all experiments. S. Q. carried out the calculation. G. S. participated in the synthesis. T. L. analyzed the single crystal data. R. Z. measured the $E_{loss}$. J. Z. and Z. W. conducted the GIWAXS. X. L., J. Z., L. M. and Y. L. supervised the project. Y. G., X. L. and Y. L. wrote the first draft. All authors commented on the previous draft and approved the final manuscript.

## Data availability

The data supporting this article are included in the ESI.†

## Conflicts of interest

The authors declare no conflict of interest.

## Acknowledgements

This work is supported by the National Key Research and Development Program of China (No. 2019YFA0705900), the National Natural Science Foundation of China (No. 21734008, 52203248, 61904181, 52103243 and 52173188), the Key Research Program of the Chinese Academy of Sciences (No. XDPB13), the Strategic Priority Research Program of the Chinese Academy of Sciences (No. XDB0520102) and the Basic and Applied Basic Research Major Program of Guangdong Province (No. 2019B030302007), and the Beijing National Laboratory for Molecular Science (2019BMS20017).

## References

1 X. Kong, C. Zhu, J. Zhang, L. Meng, S. Qin, J. Zhang, J. Li, Z. Wei and Y. Li, *Energy Environ. Sci.*, 2022, **15**, 2011–2020.
2 J. Zhang, H. Mao, K. Zhou, L. Zhang, D. Luo, P. Wang, L. Ye and Y. Chen, *Adv. Mater.*, 2023, **35**, 2309379.
3 H. Meng, W. Jing, X. Xu, L. Yu and Q. Peng, *Angew. Chem., Int. Ed.*, 2023, **62**, e202301958.
4 S. Luo, C. Li, J. Zhang, X. Zou, H. Zhao, K. Ding, H. Huang, J. Song, J. Yi, H. Yu, K. Wong, G. Zhang, H. Ade, W. Ma, H. Hu, Y. Sun and H. Yan, *Nat. Commun.*, 2023, **14**, 6964.
5 X. Zheng, L. Zuo, K. Yan, S. Shan, T. Chen, G. Ding, B. Xu, X. Yang, J. Hou, M. Shi and H. Chen, *Energy Environ. Sci.*, 2023, **16**, 2284–2294.
6 X. Wu, X. Jiang, X. Li, J. Zhang, K. Ding, H. Zhuo, J. Guo, J. Li, L. Meng, H. Ade and Y. Li, *Adv. Mater.*, 2023, **35**, 2302946.
7 Y. Cui, H. Yao, J. Zhang, K. Xian, T. Zhang, L. Hong, Y. Wang, Y. Xu, K. Ma, C. An, C. He, Z. Wei, F. Gao and J. Hou, *Adv. Mater.*, 2020, **32**, 1908205.
8 F. Lin, K. Jiang, W. Kaminsky, Z. Zhu and A. Jen, *J. Am. Chem. Soc.*, 2020, **142**, 15246–15251.
9 C. Li, J. Zhou, J. Song, J. Xu, H. Zhang, X. Zhang, J. Guo, L. Zhu, D. Wei, G. Han, J. Min, Y. Zhang, Z. Xie, Y. Yi, H. Yan, F. Gao, F. Liu and Y. Sun, *Nat. Energy*, 2021, **6**, 605–613.
10 M. Xie, Y. Shi, L. Zhu, J. Zhang, Q. Cheng, H. Zhang, Y. Yan, M. Zhu, H. Zhou, K. Lu and Z. Wei, *Energy Environ. Sci.*, 2023, **16**, 3543–3551.
11 X. Li, X. Kong, G. Sun and Y. Li, *eScience*, 2023, **3**, 100171.
12 J. Yuan, Y. Zhang, L. Zhou, G. Zhang, H. Yip, T. Lau, X. Lu, C. Zhu, H. Peng, P. Johnson, M. Leclerc, Y. Cao, J. Ulanski, Y. Li and Y. Zou, *Joule*, 2019, **3**, 1140–1151.
13 K. Liu, Y. Jiang, F. Liu, G. Ran, F. Huang, W. Wang, W. Zhang, C. Zhang, J. Hou and X. Zhu, *Adv. Mater.*, 2023, **35**, 2300363.
14 P. Bi, J. Wang, Y. Cui, J. Zhang, T. Zhang, Z. Chen, J. Qiao, J. Dai, S. Zhang, X. Hao, Z. Wei and J. Hou, *Adv. Mater.*, 2023, **35**, 2210865.
15 L. Wang, C. Chen, Y. Fu, C. Guo, D. Li, J. Cheng, W. Sun, Z. Gan, Y. Sun, B. Zhou, C. Liu, D. Liu, W. Li and T. Wang, *Nat. Energy*, 2024, **9**, 208–218.
16 S. Liu, J. Yuan, W. Deng, M. Luo, Y. Xie, Q. Liang, Y. Zou, Z. He, H. Wu and Y. Cao, *Nat. Photonics*, 2020, **14**, 300–305.
17 L. Perdigón-Toro, H. Zhang, A. Markina, J. Yuan, S. Hosseini, C. Wolff, G. Zuo, M. Stolterfoht, Y. Zou, F. Gao, D. Andrienko, S. Shoaee and D. Neher, *Adv. Mater.*, 2020, **32**, 1906763.
18 G. Zhou, M. Zhang, J. Xu, Y. Yang, T. Hao, L. Zhu, L. Zhou, H. Zhu, Y. Zou, G. Wei, Y. Zhang and F. Liu, *Energy Environ. Sci.*, 2022, **15**, 3483–3493.
19 Z. Zhang, Y. Li, G. Cai, Y. Zhang, X. Lu and Y. Lin, *J. Am. Chem. Soc.*, 2020, **142**, 18741–18745.
20 H. Chen, Y. Zou, H. Liang, T. He, X. Xu, Y. Zhang, Z. Ma, J. Wang, M. Zhang, Q. Li, C. Li, G. Long, X. Wan, Z. Yao and Y. Chen, *Sci. China: Chem.*, 2022, **65**, 1362–1373.

 

21 Y. Shi, Y. Chang, K. Lu, Z. Chen, J. Zhang, Y. Yan, D. Qiu, Y. Liu, M. Adil, W. Ma, X. Hao, L. Zhu and Z. Wei, *Nat. Commun.*, 2022, **13**, 3256.
22 Y. Guo, G. Han and Y. Yi, *Angew. Chem., Int. Ed.*, 2022, **61**, e202205975.
23 Y. Guo, L. Zhu, R. Duan, G. Han and Y. Yi, *Chem. – Eur. J.*, 2023, **29**, e202203356.
24 Y. Zhu, Z. Zhang, W. Si, Q. Sun, G. Cai, Y. Li, Y. Jia, X. Lu, W. Xu, S. Zhang and Y. Lin, *J. Am. Chem. Soc.*, 2022, **144**, 12747–12755.
25 I. Dyadishchev, A. Bakirov, S. Peregudova, S. Ponomarenko and Y. Luponosov, *Mendeleev Commun.*, 2023, **33**, 393–396.
26 Y. Xue, Z. Lai, H. Lu, J. Hong, C. Tsai, C. Huang, K. Huang, C. Lu, Y. Lai, C. Hsu, J. Lin, J. Chang, S. Chien, G. Lee, U. Jeng and Y. Cheng, *J. Am. Chem. Soc.*, 2024, **146**, 833–848.
27 Y. Xiao, J. Yuan, G. Zhou, K. Ngan, X. Xia, J. Zhu, Y. Zou, N. Zhao, X. Zhan and X. Lu, *J. Mater. Chem. A*, 2021, **9**, 17030–17038.
28 Y. Cui, P. Zhu, H. Hu, X. Xia, X. Lu, S. Yu, H. Tempeld, R. Eichel, X. Liao and Y. Chen, *Angew. Chem., Int. Ed.*, 2023, **62**, e202304931.
29 N. Hestand and F. Spano, *Chem. Rev.*, 2018, **118**, 7069–7163.
30 Z. Zhang, C. Xu, Q. Sun, Y. Zhu, W. Yan, G. Cai, Y. Li, W. Si, X. Lu, W. Xu, Y. Yang and Y. Lin, *Angew. Chem., Int. Ed.*, 2024, **63**, e202402343.
31 O. Mikhnenko, P. Blom and T. Nguyen, *Energy Environ. Sci.*, 2015, **8**, 1867–1888.
32 X. Li and Y. Li, *Acta Polym. Sin.*, 2022, **53**, 995–1004.
33 L. Ma, H. Yao, J. Wang, Y. Xu, M. Gao, Y. Zu, Y. Cui, S. Zhang, L. Ye and J. Hou, *Angew. Chem., Int. Ed.*, 2021, **60**, 15988–15994.
34 Y. Shao, T. Lu, M. Li and W. Lu, *New J. Chem.*, 2022, **46**, 3370–3382.
35 G. Han, T. Hu and Y. Yi, *Adv. Mater.*, 2020, **32**, 2000975.
36 Y. Cui, P. Zhu, X. Shi, X. Liao and Y. Chen, *J. Phys. Chem. C*, 2021, **125**, 10250–10259.
37 S. Li, L. Zhan, Y. Jin, G. Zhou, T. Lau, R. Qin, M. Shi, C. Li, H. Zhu, X. Lu, F. Zhang and H. Chen, *Adv. Mater.*, 2020, **32**, 2001160.
38 J. Zhu, Z. Qin, A. Lan, S. Jiang, J. Mou, Y. Ren, H. Do, Z. Chen and F. Chen, *Small*, 2024, **20**, 2305529.
39 C. Zhang, H. Yu, M. Zhang, X. Liu, Y. Chen, Z. Liu, Y. Wu and H. Chen, *Phys. Chem. Chem. Phys.*, 2023, **25**, 25465–25479.
40 Y. Xu, Y. Cui, H. Yao, T. Zhang, J. Zhang, L. Ma, J. Wang, Z. Wei and J. Hou, *Adv. Mater.*, 2021, **33**, 2101090.
41 X. Zhang, Y. Tang, K. Yang, P. Chen and X. Guo, *ChemElectroChem*, 2019, **6**, 5547–5562.
42 C. Liu, J. Liu, X. Duan and Y. Sun, *Adv. Sci.*, 2023, **10**, 2303842.
43 X. Yang, Y. Shao, S. Wang, M. Chen, B. Xiao, R. Sun and J. Min, *Adv. Mater.*, 2023, **35**, 2307863.
44 H. Li, S. Liu, X. Wu, S. Yao, X. Hu and Y. Chen, *Energy Environ. Sci.*, 2023, **16**, 76–88.
45 S. Li, H. Zhang, S. Yue, X. Yu and H. Zhou, *Nanotechnology*, 2022, **33**, 072002.
46 J. Yao, T. Kirchartz, M. Vezie, M. Faist, W. Gong, Z. He, H. Wu, J. Troughton, T. Watson, D. Bryant and J. Nelson, *Phys. Rev. Appl.*, 2015, **4**, 014020.
47 K. Vandewal, J. Benduhn and V. Nikolis, *Sustainable Energy Fuels*, 2018, **2**, 538–544.
48 L. Zhu, Z. Wei and Y. Yi, *J. Phys. Chem. C*, 2022, **126**, 14–21.
49 A. Mahmood and J. Wang, *Sol. RRL*, 2020, **4**, 2000337.
50 Y. Xiao and X. Lu, *Mater. Today Nano*, 2019, **5**, 100030.
51 J. Song, J. Zhan, M. Zhang, L. Zhu, T. Hao, J. Xu, Z. Zhou, G. Zhou, X. Xue, W. Feng, Y. Zhang and F. Liu, *Acta Polym. Sin.*, 2022, **53**, 1552–1566.
52 M. Gao, Z. Liang, Y. Geng and L. Ye, *Chem. Commun.*, 2020, **56**, 12463–12478.
53 C. Han, J. Wang, L. Chen, J. Chen, L. Zhou, P. Wang, W. Shen, N. Zheng, S. Wen, Y. Li and X. Bao, *Adv. Funct. Mater.*, 2021, **31**, 2107026.